Impact of molten salts composition on the corrosion behavior of NiMoCr and CoNiCrAl coatings on L-PBF 316L stainless steel for CSP plants

N. Abu-warda [*], J. Bedmar, S. García-Rodriguez, M.V. Utrilla, B. Torres, J. Rams

Dpto. de Matemática Aplicada, Ciencia e Ingeniería de Materiales y Tecnología Electrónica, ESCET, Universidad Rey Juan Carlos, Tulipán s/n, 28933 Móstoles, Madrid, Spain

ABSTRACT

The high-temperature corrosion performance of NiMoCr and CoNiCrAl coatings produced by high velocity oxy-fuel (HVOF) on laser powder bed fusion (L-PBF) 316L stainless steel substate has been evaluated in presence of three different molten salts used as thermal energy storage (TES) materials for concentrated solar power (CSP) plants. The coatings have an excellent oxidation resistance at 700 °C, showing a percentage of affected thickness lower than 2 %, due to the formation of a protective layer of Cr_2O_3 and Al_2O_3 in both NiMoCr and CoNiCrAl coatings, respectively. The carbonates-based molten salt accelerates the corrosion of the NiMoCr coating, affecting around 43 % of the coating thickness, due to the formation of chromates and the high depletion of Mo in the coating. In contrast, the effective protection shown by the CoNiCrAl coating is explained because the grown $LiAlO_2$ after the lithiation process has a high capacity to act as a strong diffusion barrier for metal ions and inhibited the formation of chromates. In the presence of two different $ZnCl_2$ and $MgCl_2$-rich molten salts, the CoNiCrAl coating behaved worse than NiMoCr coating due to the breakage of the (Al,Cr)-rich oxide layer as a consequence of an active oxidation mechanism and due to the formation of voids along the entire thickness, which were identified in 100 % of the coating thickness. The superior corrosion resistance of the NiMoCr coating in presence of the chloride rich molten salts was attributed to the presence of Mo, which fixed the Cr and inhibited the diffusion of oxygen.

1. Introduction

The use of renewable energies is becoming mandatory due to environmental issues [1]. In this context, concentrated solar power (CSP) plants have been developed in the last decades as a promising energy-generation technology [2]. Their efficiency is related to their maximum working temperature and capacity to store this energy for a time, as a significant drawback of this technology is its temporal intermittency. This issue can be solved by using different thermal energy storage (TES) materials to store the heat from sunlight in CSP plants [3,4], producing power during the absence of sunlight. TES materials add more efficiency and value to the CSP plants in this context. Molten salts are usually employed as TES materials due to their high heat storage capacity, good thermo-physical properties, and low cost [5].

The current CSP plants employ a salt mixture based on $NaNO_3$ and KNO_3, known as solar salt, with high heat capacity and low price but low thermal stability limits [6]. The maximum operating temperature of the CSP plant is limited by the stability limit of the salt, which is around

550 °C [7]. Other salts based on carbonates [8,9] or chlorides [10,11] have been proposed to overcome this operational limit. However, these salts represent a metallurgical challenge because they are much more corrosive. This added to the potential increase in the operating temperature due to the higher stability limits of the new salts, leads to an increase in the corrosion rates of the employed alloys, typically steels and Ni-base superalloys.

In this context, the use of steels in future CSP plants is limited due to the severe operating conditions. It has been observed that 316L stainless steel, in the presence of $ZnCl_2$-rich molten salts, suffers inadmissible corrosion rates for CSP applications [12]. In the same line, Ni-base superalloys are limited due to their high economic costs as bulk material in CSP plants. Therefore, a reasonable solution is using protective coatings, which minimize the cost of using expensive superalloys as bulk materials.

Different methods have been used for the manufacturing of high-temperature resistant coatings, such as sol-gel [13], plasma spray [14,15], laser-aided additive manufacturing [16], electrodeposition

* Corresponding author.
  E-mail address: najib.abuwarda@urjc.es (N. Abu-warda).

[17], high velocity oxy-fuel (HVOF) [18,19], or slurry coatings [20]. Between them, thermal spray coatings, as thus manufactured by plasma spray or HVOF, can provide suitable protection to the substrates, and particularly, the HVOF technique has been extensively used because it achieves coatings with high density and low amounts of pores and oxides. These properties are achieved in HVOF coatings because of the high velocity of the powders in the flame and the relatively low temperatures employed in the process [21]. In addition, the HVOF technique has been widely implemented by many industries, not only because of the high quality of the manufactured coatings but also because of its flexibility, cost-effectiveness, and capacity for applying coatings on-site. The coatings made by NiMoCr and CoNiCrAl made through HVOF have strongly increased resistance to the molten salts used in CSP plants on steel and Ni-based substrates [22,23].

The utilization of Laser Powder Bed Fusion (L-PBF) technology for manufacturing components in CSP plants, particularly using 316L stainless steel, presents a significant advancement in renewable energy infrastructure. L-PBF offers precise control over the fabrication process, enabling the creation of complex geometries tailored to the specific needs of CSP components, such as heat exchangers or control valves, and offers superior mechanical performance than conventional parts [24,25]. Incorporating L-PBF parts reduces the number of individual pieces and allows customization to improve the performance of CSP components. However, L-PBF 316L stainless steel also lacks resistance to the corrosive behavior of the molten salts used in CSP plants [12].

Combining L-PBF technology of 316L stainless steel with coatings applied through HVOF would enhance the performance and longevity of components in CSP plants. L-PBF enables the precise fabrication of parts, and HVOF provides high resistance to the corrosion of the substrates and enhances the durability and efficiency of components [26]. However, the conditions for the deposition of coatings on L-PBF substrates differ from those required in bulk substrates, and this means that the properties of the coatings are also different from those obtained in bulk substrates [27,28].

In this work, a substrate of 316L stainless steel manufactured by L-PBF has been coated through the HVOF technique by two different alloys based on NiMoCr and CoNiCrAl powders. These compositions have been selected due to their high performance at high temperatures [29]. The aim of the research is the characterization of the as-sprayed coatings and the analysis of their high-temperature oxidation and corrosion resistance after their exposure to three different molten salts, one based on a carbonate mixture and two based on $ZnCl_2$ and $MgCl_2$-rich chlorides, which could be used as TES materials. The results will provide helpful information about using new salt mixtures as TES materials and the possible implementation of NiMoCr and CoNiCrAl HVOF coatings in the next generation of CSP plants.

2. Experimental procedure

2.1. As-received materials

The substrate materials utilized consist of 316L austenitic stainless steel plates produced by L-PBF and supplied by Idonial Co. The composition of the powders used in the L-PBF process was 17.0 Cr, 13.1 Ni, 2.7 Mo, 1.3 Mn, 1.2 Si, $\leq$ 0.1 O, $\leq$ 0.03 C and Fe (rest) (in wt%). Substrate samples of $15 \times 15 \times 3$ mm^3 were manufactured vertically using a fiber laser EOS M280 400 W with 1070 nm wavelength, 195 W power, and 0.07 mm laser spot diameter. In addition, 1083 mm/s scanning speed, 20 μm layer height, and 90 μm hatching distance were used as processing parameters. The microstructure of the specimens was studied by and Scanning Electron Microscopy (SEM) with an accelerating voltage of 15kV using a Hitachi S-3400N microscope. The parts were cut and embedded, mechanically polished, and etched. The density of the specimens, measured following Eq. (1), was used to estimate the porosity content. The roughness was measured using a Mitutoyo SJ-210 contact profilometer.

$$\rho = \frac{W(a)[\rho(fl) - \rho(a)]}{[W(a) - W(fl)]} + \rho(a) \quad (1)$$

Flame Spray Technologies Co provided the NiMoCr and CoNiCrAl powders employed for coatings deposition, and their composition is shown in Table 1. Fig. 1 shows the SEM micrographs of the employed powders. They have the spherical morphology characteristic of the gas atomization process, which ensures the continuous powder flux through the nozzle of the HVOF gun. In addition, the powders present a heterogeneous size distribution, facilitating the formation of a dense and compact coating. The average size of the powders is $-53 + 20$ and $-45 + 22$ μm for NiMoCr and CoNiCrAl alloys, respectively.

2.2. Coatings preparation

The surface of the 316L stainless steel substrates was prepared for HVOF by sandblasting with Al_2O_3 particles of 1 mm diameter. This process increased the average roughness Ra from 2.80 ± 0.06 μm to 23.85 ± 0.39 μm and facilitated the adhesion of the metallic powder particles. The HVOF was conducted using a Sulzer Metco gun (Unicoat, DS2600) incorporated in a robotic arm (ABB IRB–2400/16). The fuel gas/oxidizing gas (H_2/O_2) ratio was 4.4, and nitrogen and dry air were used as carrier and shielding gases, respectively. In addition, the programmed parameters in the robotic arm were 250 mm spraying distance, 200 mm/s speed, 4 passes, and 10 mm line spacing. These parameters were optimized in a previous study [30] for a Ni-based coating.

The temperature, velocity, and stability of the inflight particles were monitored with an Accuraspray 4.0 (Tecnar, Canada) thermal spray sensor. The plume temperature and particle velocity are very high for both alloys ($\sim$ 2000 °C and $\sim$ 920 m/s), but the CoNiCrAl alloy is slightly more energetic, as Fig. 2 shows. These results are attributed to the high kinetic and thermal energy characteristic of the HVOF process. Furthermore, these temperature and velocity values remained remarkably stable throughout the spraying process, ensuring the formation of dense, homogeneous, and well-adhered coatings.

2.3. High-temperature corrosion tests

High-temperature corrosion tests were performed to evaluate the effect of molten salt composition on the corrosion performance of the HVOF coatings. For this purpose, three different salt mixtures have been employed. The first salt mixture is a carbonates-base salt with a composition of $35Li_2CO_3$-$33Na_2CO_3$-$32K_2CO_3$ (in wt%). The second salt mixture based on chlorides was $68MgCl_2$-$18KCl$-$14NaCl$ (in wt%), and the third was $69ZnCl_2$-$24KCl$-$7NaCl$ (in wt%). Finally, another batch of samples was tested without any salt mixture to simulate an oxidation process. These molten salts have been investigated because they are promising TES materials in CSP plants due to their low cost, low melting point, and high stability limit, as Table 2 shows [31–33]. The terminology used for each experiment, depending on the coating composition and the employed molten salt, is shown in Table 3.

Corrosion tests were performed at 700 °C for 48 h in a dry air atmosphere. The short exposure time and the non-inert atmosphere were selected to simulate a local failure in the inerting system of a CSP plant. Therefore, it is necessary to consider that these conditions are more aggressive than the normal operation conditions. In addition, the temperature was selected because it is close to the thermal stability limits of the employed salt mixtures.

Table 1
Nominal composition of the powders used in the HVOF process (in wt%).

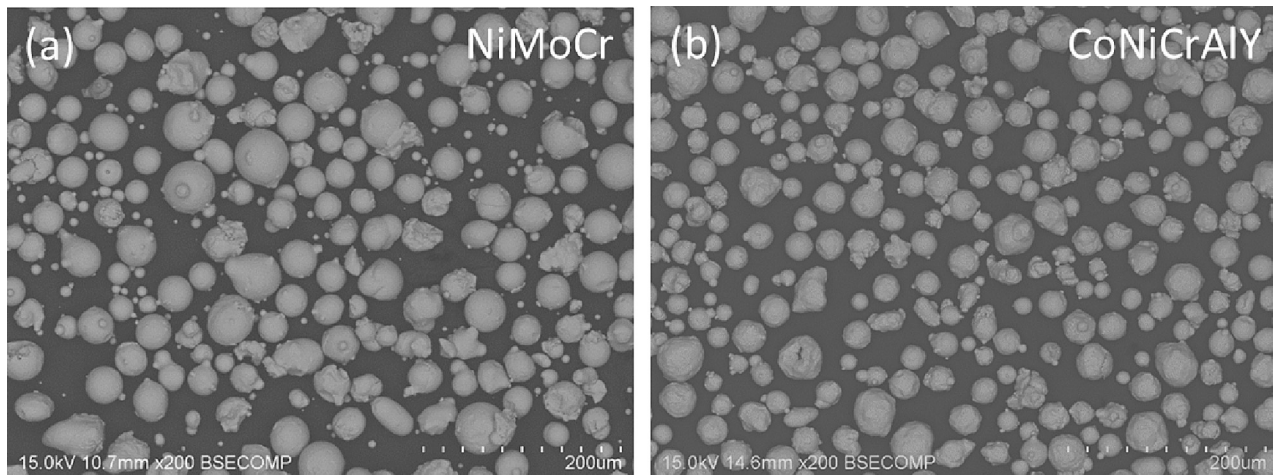| Powder nomenclature	Ni	Co	Cr	Mo	W	Fe	Al	Y
NiMoCr	Bal.	–	15.5	15.5	4	3	–	–
CoNiCrAl	32	Bal.	21	–	–	–	8	0.5

Fig. 1. SEM micrographs of the (a) NiMoCr and (b) CoNiCrAl powders used in the HVOF process.
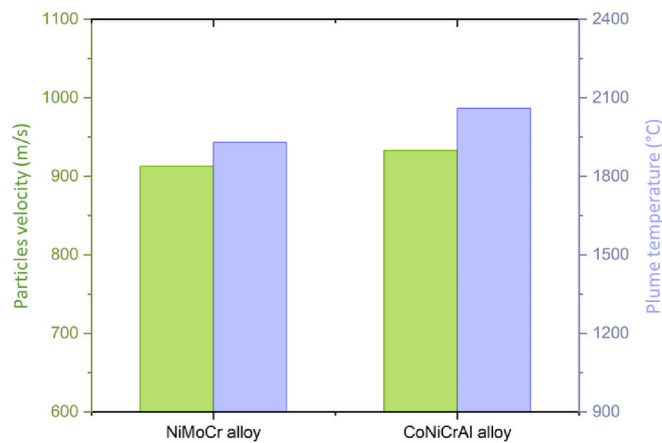

Fig. 2. Plume temperature (in °C) and particle velocity (in m/s) during the HVOF process for NiMoCr and CoNiCrAl alloys.

Table 2
Melting points and thermal stability limits of the employed molten salts.

Molten salt composition	Melting point (°C)	Thermal stability limit (°C)
Li_2CO_3-Na_2CO_3-K_2CO_3	397	>650
$ZnCl_2$-NaCl-KCl	204	850
$MgCl_2$-NaCl-KCl	380	>800

Table 3
Nomenclature used for each experiment depending on the coating composition and the employed molten solar salt.

Sample nomenclature	Coating alloy	Molten salt composition (wt%)
Ni-O	NiMoCr	Oxidation (no salts)
Ni-C	NiMoCr	$35Li_2CO_3$-$33Na_2CO_3$-$32K_2CO_3$
Ni-MgCl	NiMoCr	$68MgCl_2$-18KCl-14NaCl
Ni-ZnCl	NiMoCr	$69ZnCl_2$-24KCl-7NaCl
Co-O	CoNiCrAl	Oxidation (no salts)
Co-C	CoNiCrAl	$35Li_2CO_3$-$33Na_2CO_3$-$32K_2CO_3$
Co-MgCl	CoNiCrAl	$68MgCl_2$-18KCl-14NaCl
Co-ZnCl	CoNiCrAl	$69ZnCl_2$-24KCl-7NaCl

The coated pieces were introduced in alumina crucibles containing the different salt mixtures. A Nabertherm LT 5/12/P330 furnace was used, and at least two samples were tested for each experimental condition.

The corrosion rate produced on the HVOF coatings by the different molten salts was quantified in terms of the percentage of affected material using dimensional metrology analysis. Coatings thickness was measured before and after corrosion tests on more than forty equidistant points in each sample. Only the unaffected and uncorroded coating thickness was considered for the measurement of the remnant coating after corrosion tests. Finally, the percentage of affected coating was calculated with the difference obtained between the initial and final coating thickness.

2.4. Characterization methods

The thickness of the as-sprayed HVOF coatings was measured using a Leica/DMR optical microscope (OM) using LAS V4 Leica image analysis software. This software also measured oxides and porosity content in the as-sprayed HVOF coatings. These were estimated using the light microscope micrographs as a percentage of area with grey contrast with respect to the bright contrast of the rest of the coating area analyzed. Three micrographs of different zones of the coatings have been used to obtain average values. In addition, their roughness was measured using a Mitutoyo SJ-210 contact profilometer, and the microhardness, measured in the cross-section, was determined using an Innovatest Falcon 500 applying a load of 100 gf. At least six measurements were done in each coating at different cross-sectional depths.

The coatings were also characterized before and after corrosion tests using a Hitachi S3400N scanning electron microscope (SEM) with a Bruker XFlash 5010 X-ray dispersive energy (EDX). After high-temperature corrosion tests, the corroded samples were mounted in conductive resin and polished with diamond paste up to 3 μm using water-free lubricants to avoid the removal of water-soluble salts.

A Panalytical X'Pert PRO diffractometer was employed to analyze the composition of the oxides and corrosion products after high-temperature corrosion tests. Monochromatic KαCu (1.54 Å) was used as the radiation source with 45 kV and 40 mA. Diffraction patterns have been obtained in an angular interval of 15–90°, with the step of $\Delta(2\theta) = 0.04°$ and time per step of 1 s. The diffraction patterns have been indexed using the PDF-4 database of ICDD.

3. Results and discussion

3.1. Characterization of the substrate

316L stainless steel substrates were characterized by SEM. At low magnifications it can be observed the melt pools, produced by the laser tracks [34], and a structure free of defects, Fig. 3(a). In addition, at higher magnifications, Fig. 3(b), cellular austenitic grains can be seen,
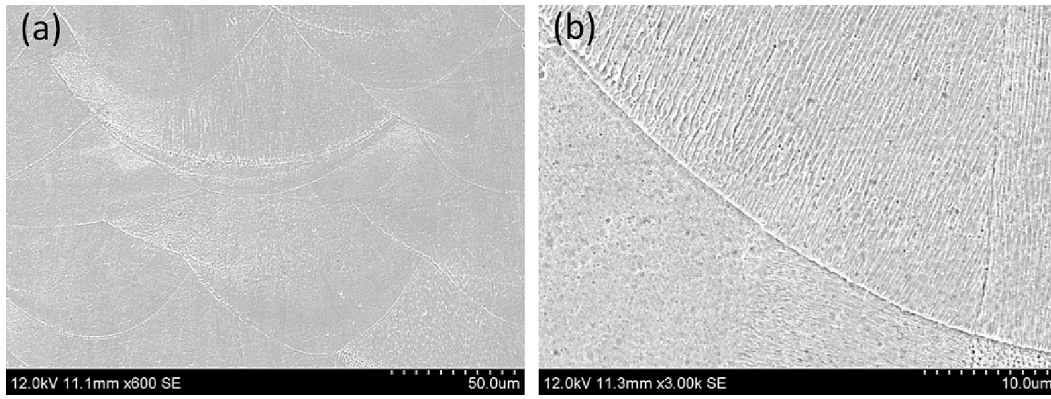
Fig. 3. Microstructure of the 316L stainless steel at (a) low magnification and at (b) high magnification.

which follow the heat gradient during the solidification process [35]. Finally, the porosity of the substrate was 0.75 % and the Ra of the substrate was 2.80 ± 0.06 μm.

3.2. HVOF coatings characterization

The morphological and compositional characterization of the NiMoCr and CoNiCrAl as-sprayed coatings has been performed through a cross-sectional SEM and an X-ray diffraction (XRD) analysis, as Fig. 4 shows. A homogeneous thickness of ~190 μm has been obtained for the NiMoCr and the CoNiCrAl coatings, as shown in Fig. 4(a) and (b), respectively. A good substrate-coating interface has been obtained (in-set magnification in Fig. 4(a)). Porosity values of 3.1 and 2.2 % were measured for the NiMoCr and CoNiCrAl coatings (red arrows marked in Fig. 3(a) and (b)), respectively, and the oxide content was ~1.7 % for both coatings. The coatings roughness (R_a) was 13 μm and 10 μm for the NiMoCr and CoNiCrAl coatings, respectively, showing minimal irregularities. The low roughness level implies that it is unlikely to

significantly impact the corrosion performance of the coatings.

The micro-hardness of the CoNiCrAl was 410 $HV_{0.1}$ and is about 10 % superior to the 369 $HV_{0.1}$ of the NiMoCr coating (Table 4). In any case, the micro-hardness of the coatings increased by 10 and 12 % compared with that of the as-received powders for the NiMoCr and CoNiCrAl, respectively. This increment is produced by the high plastic deformation induced in the powders during the deposition process.

The XRD of the as-sprayed coatings shown in Fig. 4(c) identifies the fcc-γ Ni-rich solid solution in the NiMoCr coating and the additional

Table 4
Mechanical and physical properties of the as-sprayed coatings.

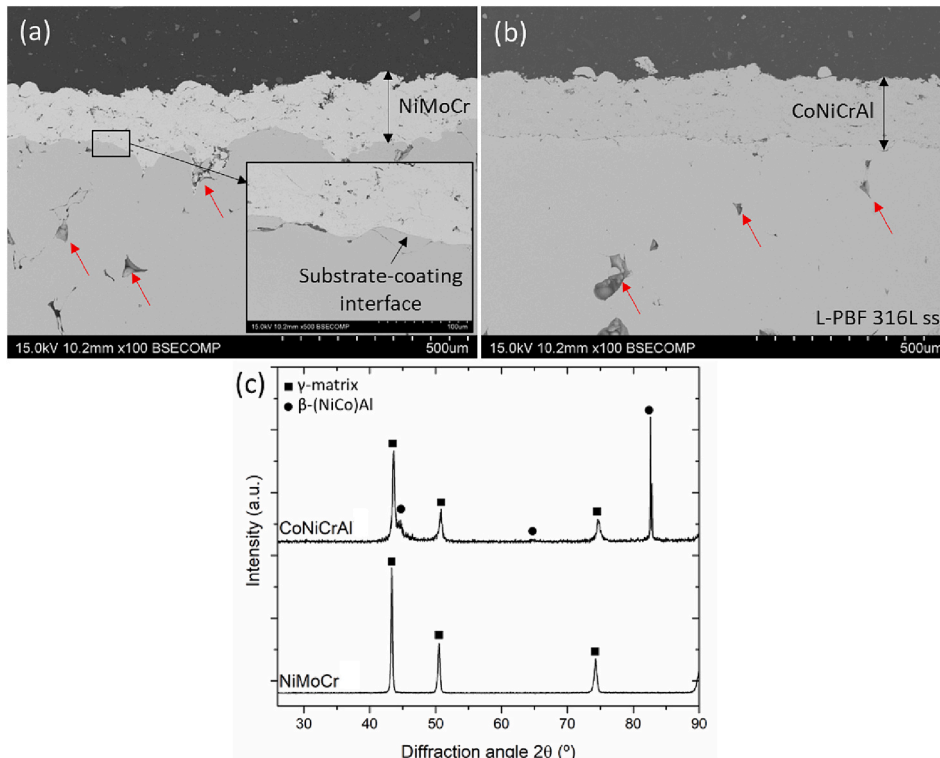| Coating	Porosity content (%)	Oxides content (%)	Average roughness Ra (μm)	Microhardness ($HV_{0.1}$)
NiMoCr	3.1 ± 0.8	1.7 ± 0.6	13 ± 1	369 ± 44
CoNiCrAl	2.2 ± 0.9	1.6 ± 0.4	10 ± 1	420 ± 15

Fig. 4. Cross-sectional SEM characterization of the as-sprayed (a) NiMoCr and (b) CoNiCrAl HVOF coatings and (c) XRD analysis.

presence of the bcc-β (Co,Ni)Al phase in the CoNiCrAl coating [36]. The presence of both fcc-γ Ni-rich and bcc-β (Co,Ni)Al phases in the CoNiCrAl coating explains its superior microhardness compared with that of the NiMoCr coating.

3.3. Corrosion tests

3.3.1. Surface characterization

The damage produced by the different salt mixtures on the surface of the coatings was first analyzed by visual examination, Fig. 5. The samples show different surface appearances depending on both the type of molten salt to which they are exposed and the coating composition.

The coatings subjected to the oxidation test exhibit a satisfactory appearance with no visible damage. The dark color of their surface is associated with the direct oxidation process, which causes the growth of protective oxides on the surface. The samples exposed to the carbonates-base molten salt show different appearance in function of coating composition and more spalled oxides are visible in the NiMoCr sample. The samples exposed to the $MgCl_2$ and $ZnCl_2$-rich molten salts show a surface full of yellow and dark corrosion products and the highest damage. However, these coated samples are much less superficially damaged compared with the uncoated 316L stainless steel substrate in the presence of $ZnCl_2$-rich molten salts, which was investigated in a previous study [12].

XRD analysis (Fig. 6) has been used to identify the principal oxides and corrosion products formed on the surface of the tested samples (Table 5). The Ni—O sample shows the prominent peaks of the γ Ni-rich solid solution and small peaks associated with $NiCr_2O_4$ (00–023-1271, ICDD) and Cr_2O_3 (01–070-3765, ICDD) oxides. In contrast, in the Co—O sample, the XRD pattern only reveals the peaks of the γ and β phases, with no additional peaks associated with the formation of oxides. This result agrees with the image shown in Fig. 5 for the Co—O sample since it does not have the dark color observed in the Ni—O sample surface. This difference indicates that the grown oxides have different compositions and a reduced thickness because of the XRD pattern did not reveal the peaks of the grown oxides.

The samples exposed to the carbonate-rich molten salts (Ni—C and Co—C) have different phases depending on the composition of the coatings. The main oxides observed on the NiMoCr coating are $NiCr_2O_4$, Cr_2O_3, and NiO (00–044-1159, ICDD). However, other non-protective corrosion products, such as K_2CrO_4 (00–001-0892, ICDD), have also been identified.

In contrast, $LiAlO_2$ (00–044-0224, ICDD) and $LiCrO_2$ (00–025-0476, ICDD) are the main corrosion products in CoNiCrAl coating, which are associated with a lithiation process. In addition, the spinel $NiAl_2O_4$ (01–077-1877, ICDD) has been identified. The presence of the γ phase in NiMoCr coating and γ-β phases in CoNiCrAl coating have also been identified, probably because the layer of grown oxides and corrosion products is thin, as the visual examination of Fig. 5 shows.

In the NiMoCr coating exposed to the $MgCl_2$-rich molten salts (Ni-MgCl), only the peaks of MgO (01–074-1225, ICDD) and $MgCr_2O_4$ (00–010-0351, ICDD) were identified, while in the CoNiCrAl coating (Co-MgCl) the peaks corresponding to MgO, $Mg(Cr,Al)_2O_4$, and Al_2O_3 (01–075-0788, ICDD)were identified. In the samples exposed to the $ZnCl_2$-rich molten salts (Co-ZnCl and Ni-ZnCl), the prominent peaks were associated with $ZnCr_2O_4$ (01–087-0028, ICDD) in both coatings, but Al_2O_3 was also formed in the CoNiCrAl coating.

3.3.2. Cross-sectional characterization

Fig. 7 shows the SEM micrographs of the NiMoCr and CoNiCrAl coatings at different magnifications after the high-temperature oxidation tests. The coatings are not damaged, as can be appreciated at low magnification in Fig. 7(a) and (c). This confirms their good oxidation resistance at 700 °C in a dry air atmosphere. Some oxides can be seen at higher magnification on their surface. In the Ni—O sample, chromia was formed, as the EDX maps of Cr, Mo, O, and Ni of Fig. 7(b) revealed, and the XRD analysis confirmed (Fig. 6). In contrast, although the XRD has not identified oxides on the CoNiCrAl coating, an Al-rich thin layer of ~2 μm thickness (Fig. 7(d)) was detected at higher magnification, as the EDX mapping of Fig. 7(e) confirmed by the presence of Al and O as the main elements in this area. According to the Gibbs free energy values reported in Eqs. (2)–(5), this oxide is formed by Al_2O_3 because its growth is more favored than other oxides such as Cr_2O_3, NiO, or CoO [37] and, in addition, its formation is more favored by the consumption of the β phase, according to Eq. (6). The high protection capacity of Al_2O_3 oxide explains the high oxidation resistance of the Co—O sample [38].

$$4/3Al + O_2 \leftrightarrows 2/3Al_2O_3 \; \Delta G^0_{Al2O3} = -900 \text{ kJ} \tag{2}$$

$$4/3Cr + O_2 \leftrightarrows 2/3Cr_2O_3 \; \Delta G^0_{Cr2O3} = -580 \text{ kJ} \tag{3}$$

$$2Co + O_2 \leftrightarrows 2CoO \; \Delta G^0_{CoO} = -330 \text{ kJ} \tag{4}$$

$$2Ni + O_2 \leftrightarrows 2NiO \; \Delta G^0_{NiO} = -310 \text{ kJ} \tag{5}$$

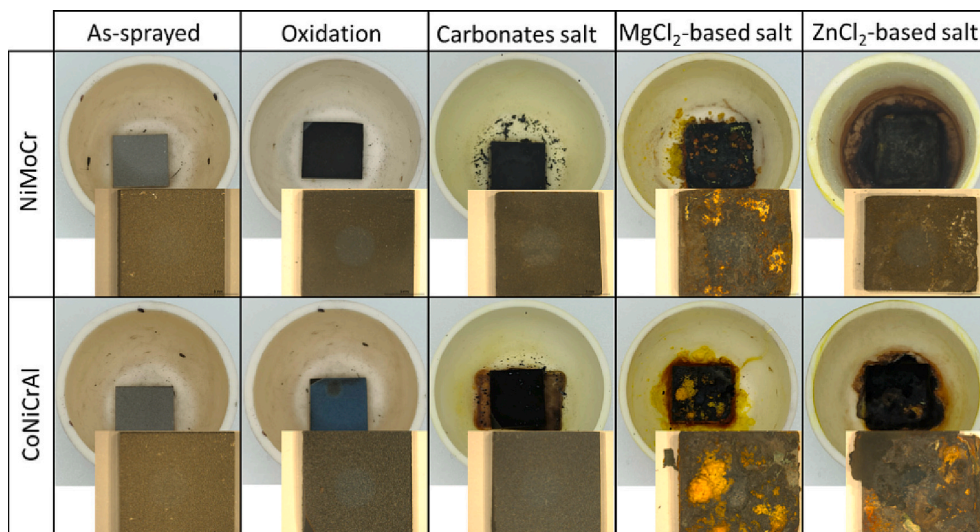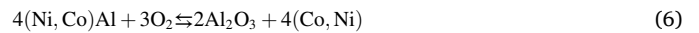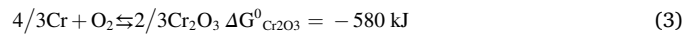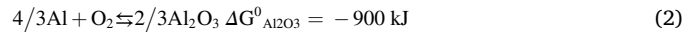$$4(Ni, Co)Al + 3O_2 \leftrightarrows 2Al_2O_3 + 4(Co, Ni) \tag{6}$$

Fig. 5. Damage analysis by visual examination of NiMoCr and CoNiCrAl HVOF coatings after oxidation and corrosion tests at 700 °C for 48 h.
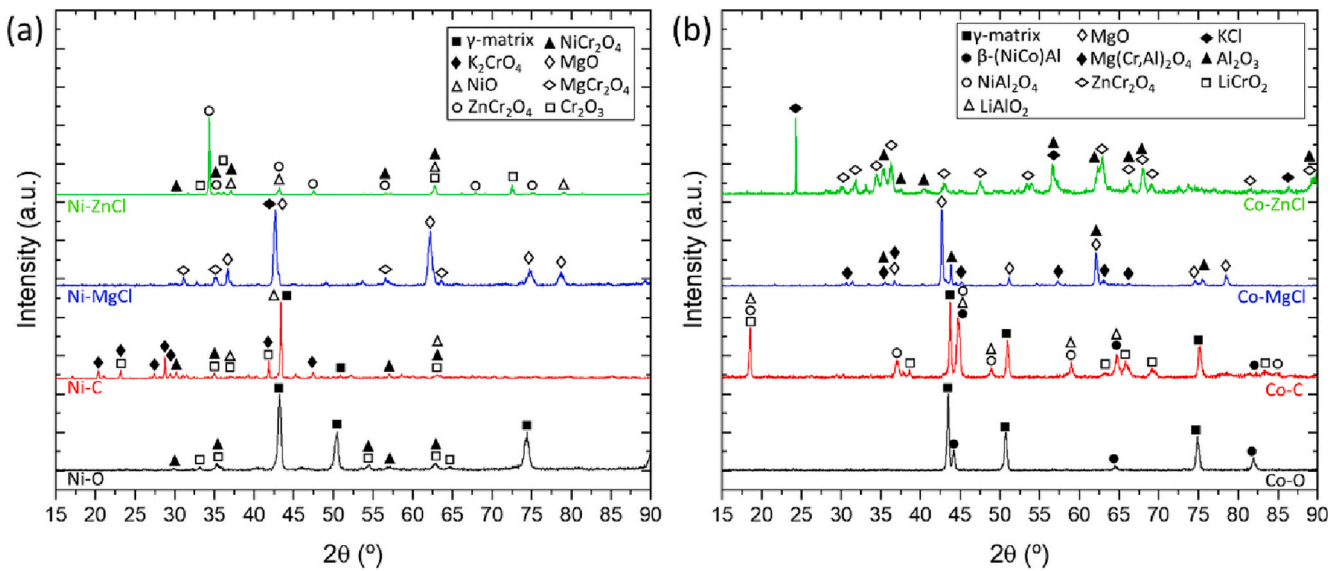
Fig. 6. XRD patterns of the (a) NiMoCr and (b) CoNiCrAl HVOF coatings after oxidation and corrosion tests at 700 °C for 48 h.

Table 5
Main phases identified by XRD in Fig. 6.

Coating	Molten salt			
	Oxidation	Carbonates	ZnCl$_2$-rich	MgCl$_2$-rich
NiMoCr	γ-Matrix	γ-Matrix	ZnCr$_2$O$_4$	MgO
	NiCr$_2$O$_4$	NiCr$_2$O$_4$	NiCr$_2$O$_4$	MgCr$_2$O$_4$
	Cr$_2$O$_3$	Cr$_2$O$_3$	Cr$_2$O$_3$	
		NiO		
		K$_2$CrO$_4$		
CoNiCrAl	γ-Matrix	γ-Matrix	ZnCr$_2$O$_4$	MgO
	β-(NiCo)Al)	β-(NiCo)Al)	Al$_2$O$_3$	Mg(Al,Cr)$_2$O$_4$
		NiAl$_2$O$_4$	KCl	Al$_2$O$_3$
		LiAlO$_2$		
		LiCrO$_2$		

The coatings exposed to the carbonates-based molten salt show a completely different behavior according to the coating composition. Fig. 8 shows the SEM micrographs of the tested coatings, and as Fig. 8(a) shows, the Ni—C sample presents a considerable area affected by the corrosion process. In contrast, the Co—C sample does not show significant damage in Fig. 8(b) at the same magnification.

The lineal EDX performed in the Ni—C sample (see Fig. 8(a)) shows the different areas that constitute the affected coating: an inner area just above the unaltered coating characterized by a high depletion of Mo and the presence of Ni—Cr spinel oxides (region III in the EDX of Fig. 8(a)); an area composed mainly by K$_2$CrO$_4$ (region II in the EDX of Fig. 8(a)); and an upper area composed mainly by Ni and O (region I in the EDX of Fig. 8(a)), probably of NiO according to the XRD of Fig. 6.

The high damage shown in the NiMoCr coating in the presence of the carbonates-based molten salts could be influenced by the formation of soluble chromates at the beginning of the corrosion process, which reduces the content of Cr in the solid solution and affects its protective capacity. The formation of the K$_2$CrO$_4$, identified in region II of Fig. 8(a), is justified according to Eq. (7).

$$Cr_2O_{3(s)} + K_2CO_{3(s)} + O_{2(g)} \leftrightarrows K_2CrO_{4(s)} + CO_{2(g)} \qquad (7)$$
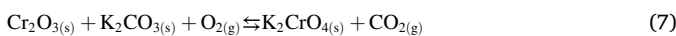
The high depletion of Mo shown in region III of Fig. 8(a) could be the main reason for the reduced protection capability of NiMoCr coating in the presence of carbonates-based molten salts. Mo diffuses from the coating to the molten carbonate, and insoluble Mo-oxides grow (Eq. (8)), then they are attacked by oxyanions (Eq. (9)) and are dissolved as molybdates [39]. De Miguel et al. [9] studied the corrosion resistance of Fe-

based and Ni-based alloys exposed to a carbonate mixture for 500 h at different temperatures in the same atmosphere, and they observed that the catastrophic behavior of the Ni-based 58Ni-23Cr-8Mo-5Fe alloy derives from the joint dissolution of Cr and Mo elements. In addition, the diffusion of Mo to the surface produces the formation of vacancies, which contribute to weakening the coating structure. They also concluded that Mo presence favors the inward diffusion of corrosive species from the melt.

$$2Mo + 3O_2 \leftrightarrows 2MoO_3 \qquad (8)$$

$$MoO_3 + O^{2-} \leftrightarrows MoO_4^{2-} \qquad (9)$$

The high corrosion resistance reported in Fig. 8(b) for the Co—C sample is justified by the formation of an Al-rich layer, as the EDX mapping of Fig. 8(c) shows at higher magnification. This protective layer isolates the coating and increases its corrosion resistance in the presence of the carbonates-base molten salts. EDX cannot detect the presence of Li, but according to the XRD of Fig. 6, this layer is composed by LiAlO$_2$, which was formed by a lithiation process due to the high activity of Li ions in the molten salts, as Eq. (10) shows [40].

$$Al_2O_3 + O^{2-} + 2Li^+ \leftrightarrows 2LiAlO_2 \qquad (10)$$

The adequate protection shown in the Co—C sample is because LiAlO$_2$ has low solubility in the molten salt and has a high capacity to act as a strong diffusion barrier for metal ions to the top of the layer, avoiding the dissolution of the protective oxides and the formation of the K$_2$CrO$_4$ identified in the Ni—C sample. Some authors [41,42] confirmed the high corrosion resistance provided by LiAlO$_2$, preventing the sample from further corrosion attack. However, this good behavior was not observed in the Ni—C sample because, in addition to the high depletion of Mo, during the lithiation process, only LiCrO$_2$ can be produced (Eq. (11)), and it has less stability and promptly reacts with carbonates and forms highly soluble chromates, as Eq. (12) shows [43]. The higher reactivity of LiCrO$_2$ with the molten salts explains why its amount on the coating surface is insufficient to be detected by XRD in the Ni—C sample and why in the EDX mapping of Fig. 8(c) the presence of Cr on the surface is neglible.
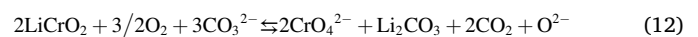
$$Cr_2O_3 + O^{2-} + 2Li^+ \leftrightarrows 2LiCrO_2 \qquad (11)$$

$$2LiCrO_2 + 3/2O_2 + 3CO_3^{2-} \leftrightarrows 2CrO_4^{2-} + Li_2CO_3 + 2CO_2 + O^{2-} \qquad (12)$$

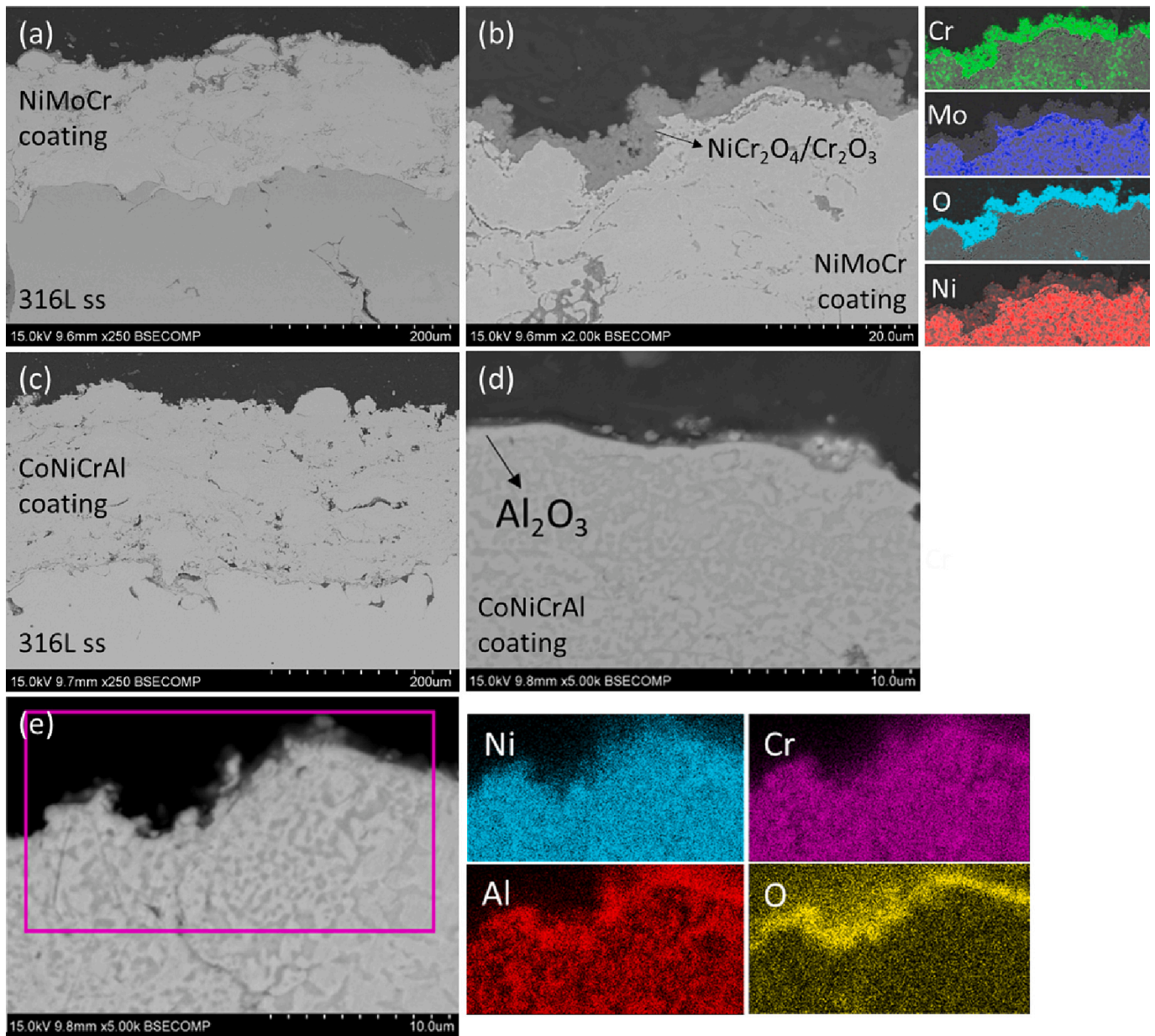Fig. 9 shows the SEM micrographs of Ni-ZnCl and Co-ZnCl samples at

Fig. 7. SEM micrographs and EDX analysis of (a, b) NiMoCr and (c–e) CoNiCrAl coatings after high-temperature oxidation tests at 700 °C for 48 h.

different magnifications after exposure to the ZnCl$_2$-rich salt mixture at 700 °C for 48 h, and differences in the corrosion resistance of both coatings have been observed. Fig. 9(a) shows at low magnification that the surface of the Ni-ZnCl sample is full of salts and corrosion products (region I in Fig. 9(b)) and that the coating has maintained its integrity, as region III of Fig. 9(b) shows and the lineal EDX of Fig. 9(c) confirms. However, in the coating-corrosion products interface (region II of Fig. 9 (b) and (c)), a homogeneous corrosion process was produced. Some coating corrosion was caused by chlorine, as shown by the lineal EDX of Fig. 9(c) in region II.

The presence of ZnCl$_2$ in the molten salt induced an active oxidation mechanism of the NiMoCr coating; the chlorides react with the metal oxides and form chlorine according to Eq. (13). Then, chlorine reacts with alloying elements to form metal chlorides such as CrCl$_3$, and finally, the chlorides react again with O$_2$ to form chlorine, restarting the process again, as Eqs. (14)–(15) show.

$$ZnCl_2 + Cr_2O_3 + 1/2O_2 \leftrightarrows ZnCr_2O_4 + Cl_2 \tag{13}$$

$$Cr_{(s)} + 3/2Cl_{2(g)} \leftrightarrows CrCl_{3(s)} \; \Delta G^0_{(CrCl3)} = -371.6 \text{ kJ} \tag{14}$$

$$2CrCl_{3(g)} + 3/2O_{2(g)} \leftrightarrows Cr_2O_{3(s)} + 3Cl_{2(g)} \; \Delta G^0_{(Cr2O3)} = -255.6 \text{ kJ} \tag{15}$$
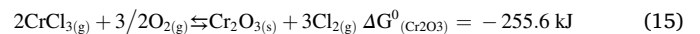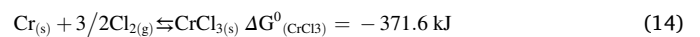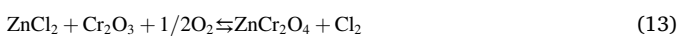
Fig. 9(d) shows the cross-section micrograph of the Co-ZnCl sample and the lineal EDX analysis of its surface, and Fig. 9(e) shows a magnification of the top zone of the coating where porosity can be observed. The number of voids shown in the coating is superior to that observed in the as-sprayed coating because of the Kirkendall effect caused by the high diffusion rates of some alloying elements, such as Cr and Al.

The linear EDX shown in Fig. 9(f) corresponds to the allow marked in Fig. 9(d), and three different areas of the coating can be distinguished: an upper area mainly composed of Al and O (region I), an inner area just above the coating mainly composed of Cr, Cl, and O (region II), and the coating itself (region III).

The depletion of Al from the coating was caused by the displacement reaction with ZnCl$_2$ from the melt shown in Eq. (16), which promotes
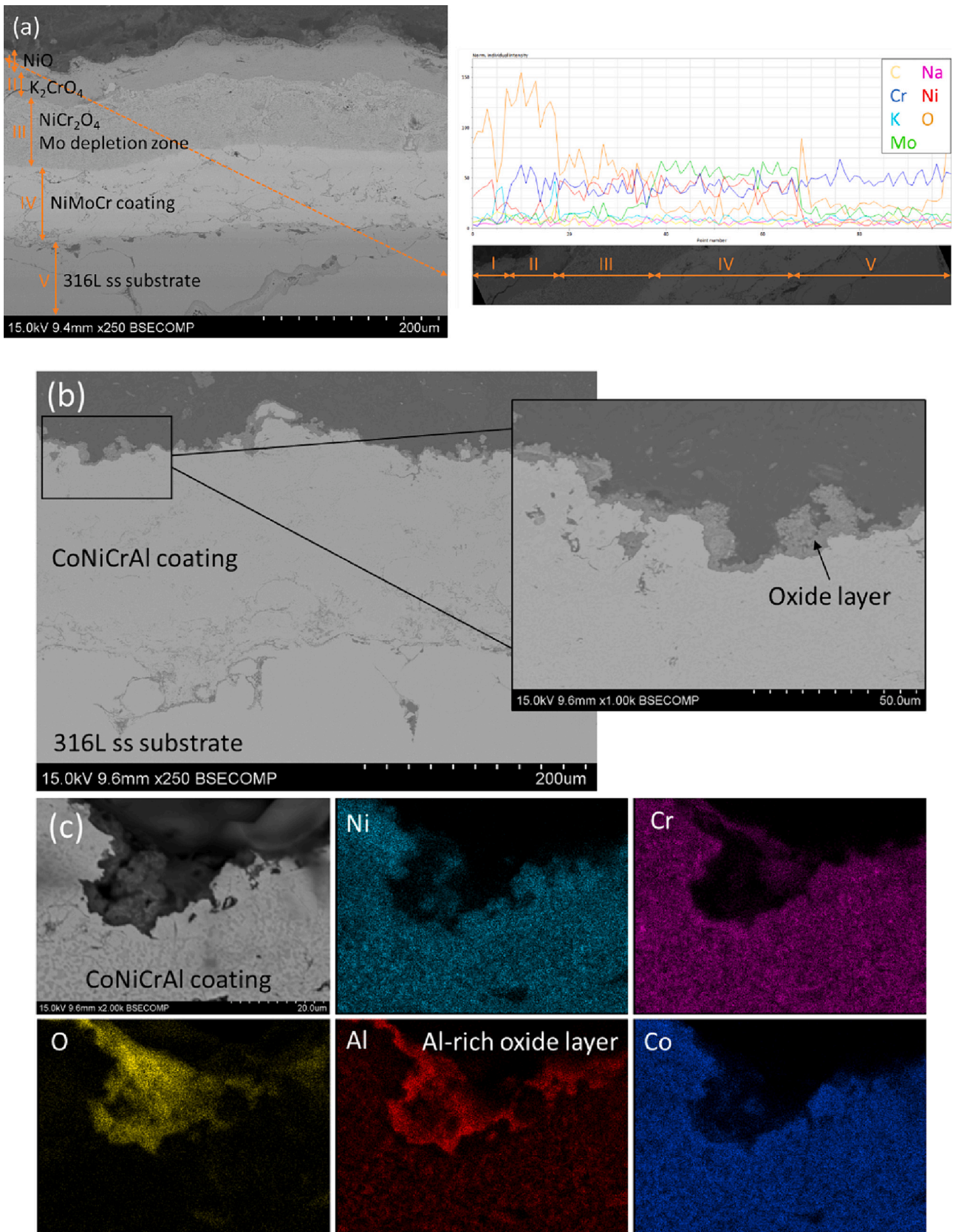
Fig. 8. Cross-sectional SEM micrographs and EDX analysis of (a) NiMoCr and (b–c) CoNiCrAl coatings after high-temperature corrosion in the presence of carbonates-based molten salts at 700 °C for 48 h.
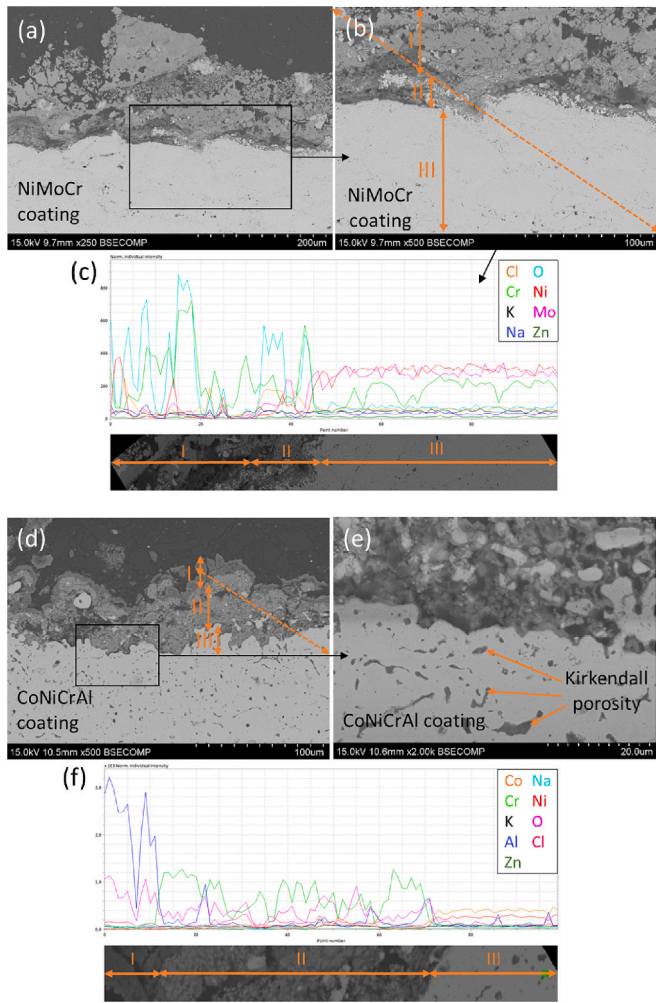
Fig. 9. Cross-sectional SEM micrographs and EDX analysis of (a–c) NiMoCr and (d–f) CoNiCrAl coatings after high-temperature corrosion in the presence of $ZnCl_2$-based molten salts at 700 °C for 48 h.
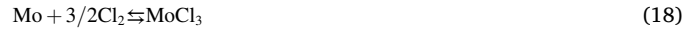
the formation of $AlCl_3$ [44]. Subsequently, the oxidation of aluminum chlorides, described in Eq. (17), leads to forming a porous Al_2O_3 layer that constitutes the region I in the EDX (Fig. 9(f)). This cyclic process produces the excessive depletion of the protective elements from the coating and the formation of the voids. The presence of these voids contributes to the weakening of the coating structure but does not cause its dissolution.

$$3ZnCl_2 + 2Al \leftrightharpoons 3Zn + 2AlCl_3 \qquad (16)$$

$$2AlCl_3 + 3/2O_2 \leftrightharpoons Al_2O_3 + 3Cl_2 \qquad (17)$$

The two coatings studied show distinct behavior against the $MgCl_2$-rich molten salt, and the corrosion process was more severe in the CoNiCrAl coating than in the NiMoCr. The main degradation was caused by the chloride attack and the formation of voids due to the diffusion of some alloying elements to the surface, as Fig. 10 shows. In the Ni-MgCl sample, small voids were formed only in the splat particle boundaries, while in the Co-MgCl sample, they were bigger and formed across the thickness of the coating.

In contrast with the Ni—C sample, the greater corrosion resistance shown in the NiMoCr coating is because of the presence of Mo, which produced the fixation of Cr in the coating and reduced oxygen diffusion [45]. Thermodynamically, the formation of $CrCl_4$ is more favored than $MoCl_3$, according to Eqs. (18)–(19). Once the $MoCl_3$ forms, its transformation to MoO_3 is more thermodynamically favored than the

transformation of $CrCl_4$ to Cr_2O_3, Eqs. (20)–(21) [46]. This causes the appearance of fine voids in the splat boundaries shown in Fig. 10(b) because of the volatilization of $CrCl_4$. This mechanism explains that Mo presence in the oxide scale provides better corrosion protection.

$$Mo + 3/2Cl_2 \leftrightharpoons MoCl_3 \qquad (18)$$

$$Cr + 2Cl_2 \leftrightharpoons CrCl_4 \qquad (19)$$

$$MoCl_3 + 3/2O_2 \leftrightharpoons MoO_3 + 3/2Cl_2 \qquad (20)$$

$$2CrCl_4 + 3/2O_2 \leftrightharpoons Cr_2O_3 + 4Cl_2 \qquad (21)$$

A previous work analyzed the high-temperature corrosion behavior of two Ni-based coatings with different Mo contents (0 and 15.5 wt%) in a NaCl-KCl salt mixture [29]. The results showed that the diffusion of Cr to the splat boundaries was more limited in the Mo-rich sample, and this is also observed in this work comparing Ni-MgCl and Co-MgCl samples, Fig. 10(a) and (c), respectively.

In addition, the main corrosion products of the Ni-MgCl sample were MgO and $MgCr_2O_4$. These oxides were formed due to the high reactivity of the Mg with the oxygen and alloying elements, particularly Cr. In the presence of traces of water, $MgCl_2$ can absorb moisture to form hydroxyl magnesium chloride, following Eqs. (22)–(25) [47].

$$Mg^{2+} + H_2O + Cl^- \leftrightharpoons MgOH^+ + HCl \qquad (22)$$

$$MgOH^+ \leftrightharpoons MgO + HCl \qquad (23)$$

$$MgCl_2 + H_2O \leftrightharpoons MgO + 2\,HCl \qquad (24)$$

$$MgO + Cr_2O_3 \leftrightharpoons MgCr_2O_4 \qquad (25)$$

The main corrosion products in the CoNiCrAl coating were MgO and $Mg(Al,Cr)_2O_4$, but also Al_2O_3, according to the XRD of Fig. 6. Voids appeared across the coating and a dual-layer of $Mg(Al,Cr)_2O_4$ on the top and Al_2O_3 on the bottom with a thickness of ~25 μm formed on the surface. This layer presented breaks, red circles in Fig. 10(c), so it does not fully isolate the coating from the molten salts. However, the corrosion process did not affect the 316L stainless steel substrate despite the appearance of voids across the entire CoNiCrAl coating.

3.3.3. Quantification of the corrosion process

The corrosion produced by the different salt mixtures in the coatings has been quantified by measuring the percentage of affected coating on their transversal section and the results are plotted in Fig. 11. The percentage of affected thickness in NiMoCr and CoNiCrAl coatings exposed to air at 700 °C for 48 h is negligible (< 2 %), showing that both have high resistance to direct oxidation mechanism under this experimental condition.

In the coatings exposed to carbonate salts, i.e., Ni—C and Co—C tests, the percentage of affected thickness for the CoNiCrAl coating was 4 %, while it was 43 % for the NiMoCr one. This confirms that the CoNiCrAl coating has a much superior corrosion resistance than the NiMoCr coating. The lithiation process influences the percentage of affected material in both coatings, but the higher corrosion rates shown in NiMoCr coating are mainly associated with Mo-depletion and the absence of a protective $LiAlO_2$ layer as that grown in the CoNiCrAl coating.

The samples exposed to $ZnCl_2$ and $MgCl_2$-rich molten salts show the highest corrosion rates. The presence of chlorides in the molten salt induced an active oxidation mechanism in the coatings due to the reaction of the chlorides with the metal oxides producing the formation of chlorine, then chlorine reacts with alloying elements to form metal chlorides, restarting the process again. However, in contrast with the results reported for the coatings exposed to the carbonates-base molten salt, the CoNiCrAl coating was more affected than the NiMoCr in the presence of chloride-rich molten salts. The 100 % of Co-ZnCl and Co-
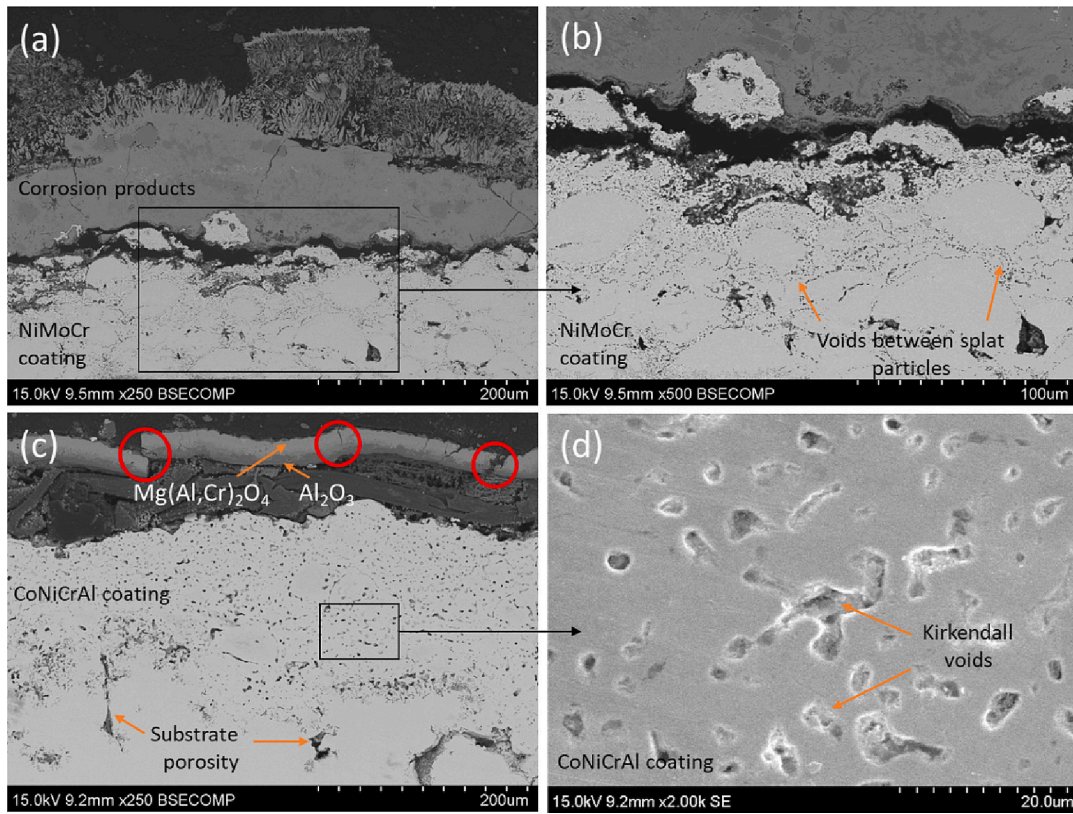
Fig. 10. Cross-sectional SEM micrographs at different magnifications of (a–b) NiMoCr and (c–d) CoNiCrAl coatings after high-temperature corrosion in the presence of MgCl$_2$-based molten salts at 700 °C for 48 h.
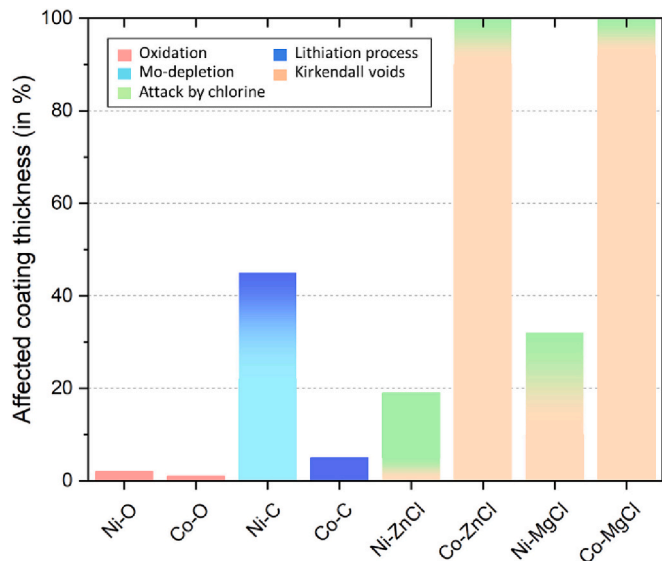

Fig. 11. Percentage of affected coating thickness and degradation mechanism depending on coating and salt composition.

MgCl samples thickness was affected, and the appearance of Kirkendall voids represents 90 % and 92 % of the affected thickness. This is attributed to the excessive depletion of the protective elements from the coating and is considered the main degradation mechanism for this coating. However, in these CoNiCrAl samples, a low percentage of the affected thickness (10 % and 8 %, respectively) was attributed to the attack by chlorine. In contrast, Ni-ZnCl sample only had 19 % of its thickness affected by the corrosion process (5 % attributed to the

presence of voids and 14 % to the attack by chlorine). In the same line, Ni-MgCl sample had 32 % of its thickness affected by the corrosion process (10 % attributed to the presence of voids and 22 % to the attack by chlorine). In these NiMoCr samples the predominant degradation process was associated to an active oxidation mechanism rather than to the formation of voids in the inner areas.

It can be concluded that depending on the molten salt composition, it will be suitable to use a type of coating or other. If a carbonate-based salt is used, it will be more suitable to use coatings with a higher Al concentration and less Mo concentration. On the contrary, if a chloride-rich molten salt is used, it will be more suitable to use coatings with Mo to fix the alloying elements such as Cr or Al in the alloy. In any case, no damage on the L-PBF 316L stainless steel substrate was observed in any of the analyzed conditions, even in the samples in which 100 % of coating thickness was affected due to the formation of voids. These results demonstrate that combining L-PBF technology of 316L substrate with HVOF coatings would enhance the performance and longevity of components with complex geometries tailored to the specific needs of CSP plants.

4. Conclusions

- The as-sprayed NiMoCr and CoNiCrAl coatings have an excellent substrate-coating interface with low oxides and porosity content.
- The type of molten salt and coating composition greatly influences the high-temperature corrosion resistance.
- The high oxidation resistance of both NiMoCr and CoNiCrAl coatings is due to the formation of a protective layer of Cr$_2$O$_3$ and Al$_2$O$_3$, respectively.
- The high damage shown in the NiMoCr coating in the presence of the carbonates-based molten salts could be influenced by the formation of soluble chromates and the high depletion of Mo. The effective protection shown in the CoNiCrAl coating is because the grown

LiAlO$_2$ has a high capacity to act as a strong diffusion barrier for metal ions.

- In the presence of two different ZnCl$_2$ and MgCl$_2$-rich molten salts, the CoNiCrAl coating behaved worse due to the breakage of the (Al, Cr)-rich oxide layer as a consequence of an active oxidation mechanism and due to the formation of Kirkendall voids. The superior corrosion resistance of the NiMoCr coating was attributed to the presence of Mo, which fixed the Cr and inhibited the diffusion of oxygen.
- No damage on the L-PBF 316L stainless steel substrate was observed in any of the analyzed conditions.

CRediT authorship contribution statement

N. Abu-warda: Writing – review & editing, Writing – original draft, Methodology, Investigation, Formal analysis, Conceptualization. **J. Bedmar:** Writing – review & editing, Methodology, Formal analysis, Conceptualization. **S. García-Rodriguez:** Writing – review & editing, Methodology, Formal analysis, Conceptualization. **M.V. Utrilla:** Writing – review & editing, Supervision. **B. Torres:** Writing – review & editing, Supervision, Funding acquisition. **J. Rams:** Writing – review & editing, Supervision, Project administration, Funding acquisition.

Declaration of competing interest

The authors declare that they have no known competing financial interests or personal relationships that could have appeared to influence the work reported in this paper.

Data availability

The raw/processed data required to reproduce these findings cannot be shared at this time due to technical limitations.

Acknowledgments

References

[1] M. Walczak, F. Pineda, Á.G. Fernández, C. Mata-Torres, R.A. Escobar, Materials corrosion for thermal energy storage systems in concentrated solar power plants, Renew. Sust. Energ. Rev. 86 (2018) 22–44, https://doi.org/10.1016/j.rser.2018.01.010.

[2] K. Vignarooban, X. Xu, A. Arvay, K. Hsu, A.M. Kannan, Heat transfer fluids for concentrating solar power systems – a review, Appl. Energy 146 (2015) 383–396, https://doi.org/10.1016/j.apenergy.2015.01.125.

[3] A. Gomes, M. Navas, N. Uranga, T. Paiva, I. Figueira, T.C. Diamantino, High-temperature corrosion performance of austenitic stainless steels type AISI 316L and AISI 321H, in molten solar salt, Sol. Energy 177 (2019) 408–419, https://doi.org/10.1016/j.solener.2018.11.019.

[4] U. Pelay, L. Luo, Y. Fan, D. Stitou, M. Rood, Thermal energy storage systems for concentrated solar power plants, Renew. Sust. Energ. Rev. 79 (2017) 82–100, https://doi.org/10.1016/j.rser.2017.03.139.

[5] X. Xu, G. Dehghani, J. Ning, P. Li, Basic properties of eutectic chloride salts NaCl-KCl-ZnCl2 and NaCl-KCl-MgCl2 as HTFs and thermal storage media measured using simultaneous DSC-TGA, Sol. Energy 162 (2018) 431–441, https://doi.org/10.1016/j.solener.2018.01.067.

[6] Á.G. Fernández, L.F. Cabeza, Molten salt corrosion mechanisms of nitrate based thermal energy storage materials for concentrated solar power plants: a review, Sol. Energy Mater. Sol. Cells 194 (2019) 160–165, https://doi.org/10.1016/j.solmat.2019.02.012.

[7] H. Li, X. Feng, X. Wang, X. Yang, J. Tang, J. Gong, Impact of temperature on corrosion behavior of austenitic stainless steels in solar salt for CSP application: an electrochemical study, Sol. Energy Mater. Sol. Cells 239 (2022) 111661, https://doi.org/10.1016/j.solmat.2022.111661.

[8] J. Luo, C.K. Deng, N. ul H. Tariq, N. Li, R.F. Han, H.H. Liu, J.Q. Wang, X.Y. Cui, T.Y. Xiong, Corrosion behavior of SS316L in ternary Li2CO3–Na2CO3–K2CO3 eutectic mixture salt for concentrated solar power plants, Sol. Energy Mater. Sol. Cells 217 (2020), https://doi.org/10.1016/j.solmat.2020.110679.

[9] M.T. de Miguel, M.I. Lasanta, G. García-Martín, R. Díaz, F.J. Pérez, Temperature effect and alloying elements impact on the corrosion behaviour of the alloys exposed to molten carbonate environments for CSP application, Corros. Sci. 201 (2022), https://doi.org/10.1016/j.corsci.2022.110274.

[10] Q. Liu, H. Xu, H. Yin, N. Li, W. Wang, L. Li, Z. Tang, Y. Qian, Corrosion behaviour of 316 stainless steel in NaCl-KCl-MgCl2 salt vapour at 700°C, Corros. Sci. 194 (2022), https://doi.org/10.1016/j.corsci.2021.109921.

[11] M. Wang, S. Zeng, H. Zhang, M. Zhu, C. Lei, B. Li, Corrosion behaviors of 316 stainless steel and Inconel 625 alloy in chloride molten salts for solar energy storage, High Temp. Mater. Process. 39 (2020) 340–350, https://doi.org/10.1515/htmp-2020-0077.

[12] N. Abu-warda, S. García-Rodríguez, B. Torres, M.V. Utrilla, J. Rams, Impact of the additive manufacturing process on the high-temperature corrosion of 316L steel in the presence of NaCl-KCl ZnCl2 molten solar salt, J. Mater. Res. Technol. (2022), https://doi.org/10.1016/j.jmrt.2022.08.140.

[13] V. Encinas-Sánchez, E. Batuecas, A. Macías-García, C. Mayo, R. Díaz, F.J. Pérez, Corrosion resistance of protective coatings against molten nitrate salts for thermal energy storage and their environmental impact in CSP technology, Sol. Energy 176 (2018) 688–697, https://doi.org/10.1016/j.solener.2018.10.083.

[14] F. Kirbiyik, M.G. Gok, G. Goller, Recent Developments on Al2O3-based Thermal Barrier Coatings, 2024, pp. 125–150, https://doi.org/10.1007/978-3-031-40809-0_4.

[15] F. Kirbiyik, M.G. Gok, G. Goller, Application of thermal gradient and thermal cycling tests to Al2O3/CYSZ functionally graded TBC in the presence of simultaneous hot corrosion and CMAS effects, Surf. Coat. Technol. 444 (2022) 128688, https://doi.org/10.1016/j.surfcoat.2022.128688.

[16] M. Ansari, R. Shoja-Razavi, M. Barekat, H.C. Man, High-temperature oxidation behavior of laser-aided additively manufactured NiCrAlY coating, Corros. Sci. 118 (2017) 168–177, https://doi.org/10.1016/j.corsci.2017.02.001.

[17] T.M. Meißner, C. Oskay, A. Bonk, B. Grégoire, A. Donchev, A. Solimani, M.C. Galetz, Improving the corrosion resistance of ferritic-martensitic steels at 600 °C in molten solar salt via diffusion coatings, Sol. Energy Mater. Sol. Cells 227 (2021), https://doi.org/10.1016/j.solmat.2021.111105.

[18] G. Binal, Isothermal oxidation and hot corrosion behavior of HVOF sprayed 80Ni-20Cr coatings at 750 °C, Surf. Coat. Technol. 454 (2023) 129141, https://doi.org/10.1016/j.surfcoat.2022.129141.

[19] M.G. Gok, G. Goller, Microstructural characterization of GZ/CYSZ thermal barrier coatings after thermal shock and CMAS+hot corrosion test, J. Eur. Ceram. Soc. 37 (2017) 2501–2508, https://doi.org/10.1016/j.jeurceramsoc.2017.02.004.

[20] P. Audigié, V. Encinas-Sánchez, M. Juez-Lorenzo, S. Rodríguez, M. Gutiérrez, F.J. Pérez, A. Agüero, High temperature molten salt corrosion behavior of aluminide and nickel-aluminide coatings for heat storage in concentrated solar power plants, Surf. Coat. Technol. 349 (2018) 1148–1157, https://doi.org/10.1016/j.surfcoat.2018.05.081.

[21] N. Abu-warda, A.J. López, M.D. López, M.V. Utrilla, Ni20Cr coating on T24 steel pipes by HVOF thermal spray for high temperature protection, Surf. Coat. Technol. 381 (2020), https://doi.org/10.1016/j.surfcoat.2019.125133.

[22] K. Yuan, R. Lin Peng, X.H. Li, S. Johansson, Hot corrosion behavior of HVOF-sprayed CoNiCrAlYSi coatings in a sulphate environment, Vacuum 122 (2015) 47–53, https://doi.org/10.1016/j.vacuum.2015.09.015.

[23] H. Chen, Microstructure characterisation of un-melted particles in a plasma sprayed CoNiCrAlY coating, Mater. Charact. 136 (2018) 444–451, https://doi.org/10.1016/j.matchar.2017.09.020.

[24] M. Xu, H. Guo, Y. Wang, Y. Hou, Z. Dong, L. Zhang, Mechanical properties and microstructural characteristics of 316L stainless steel fabricated by laser powder bed fusion and binder jetting, J. Mater. Res. Technol. 24 (2023) 4427–4439, https://doi.org/10.1016/j.jmrt.2023.04.069.

[25] D. Herzog, V. Seyda, E. Wycisk, C. Emmelmann, Additive manufacturing of metals, Acta Mater. 117 (2016) 371–392, https://doi.org/10.1016/j.actamat.2016.07.019.

[26] W. Tillmann, L. Hagen, C. Schaak, J. Liß, M. Schaper, K.-P. Hoyer, M.E. Aydinöz, K.-U. Garthe, Adhesion of HVOF-sprayed WC-Co coatings on 316L substrates processed by SLM, J. Therm. Spray Technol. 29 (2020) 1396–1409, https://doi.org/10.1007/s11666-020-01081-y.

[27] D.M. Jafarlou, G. Ferguson, K.L. Tsaknopoulos, A.C. Chuang, A. Nardi, D. Cote, V. Champagne, I.R. Grosse, Structural integrity of additively manufactured stainless steel with cold sprayed barrier coating under combined cyclic loading, Addit. Manuf. 35 (2020) 101338, https://doi.org/10.1016/j.addma.2020.101338.

[28] G. Bolelli, M.F. Bonilauri, P. Sassatelli, F. Bruno, R. Franci, G. Pulci, F. Marra, L. Paglia, G.C. Gazzadi, S. Frabboni, L. Lusvarghi, Pre-treatment of Selective Laser Melting (SLM) surfaces for thermal spray coating, Surf. Coat. Technol. 441 (2022) 128533, https://doi.org/10.1016/j.surfcoat.2022.128533.

[29] N. Abu-warda, L.M. Tomás, A.J. López, M.V. Utrilla, High temperature corrosion behavior of Ni and Co base HVOF coatings exposed to NaCl-KCl salt mixture, Surf. Coat. Technol. 418 (2021), https://doi.org/10.1016/j.surfcoat.2021.127277.

[30] N. Abu-warda, G. Boissonnet, A.J. López, M.V. Utrilla, F. Pedraza, Analysis of thermo-physical properties of NiCr HVOF coatings on T24, T92, VM12 and AISI 304 steels, Surf. Coat. Technol. 416 (2021), https://doi.org/10.1016/j.surfcoat.2021.127163.

[31] An, X.-H.; Cheng, J.-H.; Su, T.; Zhang, P. Determination of thermal physical properties of alkali fluoride/carbonate eutectic molten salt. In AIP Conference Proceedings; AIP Publishing LLC: Melville, NY, USA, 2017; Volume 1850, p. 070001., (n.d.).

[32] Du, L.; Ding, J.; Tian, H.; Wang, W.; Wei, X.; Song, M. Thermal properties and thermal stability of the ternary eutectic salt NaCl-CaCl2-MgCl2 used in high-temperature thermal energy storage process. Appl. Energy 2017, 204, 1225–1230., (n.d.).

[33] Y. Li, X. Xu, X. Wang, P. Li, Q. Hao, B. Xiao, Survey and evaluation of equations for thermophysical properties of binary/ternary eutectic salts from NaCl, KCl, MgCl2, CaCl2, ZnCl2 for heat transfer and thermal storage fluids in CSP, Sol. Energy n.d. (2017).

[34] Y. Chen, C. Liu, H. Yan, Y. Fan, J. Wang, Y. Cui, Effect of gas nitriding on 316 L stainless steel lattice manufactured via selective laser melting, Surf. Coat. Technol. 441 (2022) 128559, https://doi.org/10.1016/j.surfcoat.2022.128559.

[35] A. Evangelou, R. Stylianou, A. Loizou, D. Kim, A. Liang, P. Reed, G. Constantinides, T. Kyratsi, Effects of process parameters and scan strategy on the microstructure and density of stainless steel 316 L produced via laser powder bed fusion, J. Alloy. Metall. Syst. 3 (2023) 100027, https://doi.org/10.1016/j.jalmes.2023.100027.

[36] H. Chen, T.H. Hyde, K.T. Voisey, D.G. McCartney, Application of small punch creep testing to a thermally sprayed CoNiCrAlY bond coat, Mater. Sci. Eng. A 585 (2013) 205–213, https://doi.org/10.1016/j.msea.2013.06.080.

[37] Y. Han, Z. Zhu, B. Zhang, Y. Chu, Y. Zhang, J. Fan, Effects of process parameters of vacuum pre-oxidation on the microstructural evolution of CoCrAlY coating deposited by HVOF, J. Alloys Compd. 735 (2018) 547–559, https://doi.org/10.1016/j.jallcom.2017.11.165.

[38] A.S. Khanna, W.S. Rathod, Development of CoNiCrAlY oxidation resistant hard coatings using high velocity oxy fuel and cold spray techniques, Int. J. Refract. Met. Hard Mater. 49 (2015) 374–382, https://doi.org/10.1016/j.ijrmhm.2014.08.010.

[39] F.J. Pérez, E. Otero, M.P. Hierro, C. Gómez, F. Pedraza, J.L. De Segovia, E. Román, High temperature corrosion protection of austenitic AISI 304 stainless steel by Si, Mo and Ce ion implantation, Surf. Coat. Technol. 108–109 (1998) 127–131, https://doi.org/10.1016/S0257-8972(98)00685-9.

[40] J. Luo, N. ul H. Tariq, H.H. Liu, N. Li, L.J. Zhao, X.Y. Cui, T.Y. Xiong, Robust corrosion performance of cold sprayed aluminide coating in ternary molten carbonate salt for concentrated solar power plants, Sol. Energy Mater. Sol. Cells 237 (2022) 111573, https://doi.org/10.1016/j.solmat.2021.111573.

[41] J.G. Gonzalez-Rodriguez, E. Mejia, M.A. Lucio-Garcia, V.M. Salinas-Bravo, J. Porcayo-Calderon, A. Martinez-Villafañe, An electrochemical study of the effect of Li on the corrosion behavior of Ni3Al intermetallic alloy in molten (Li+K) carbonate, Corros. Sci. 51 (2009) 1619–1627, https://doi.org/10.1016/j.corsci.2009.04.012.

[42] J. Jun, Degradation behaviour of Al–Fe coatings in wet-seal area of molten carbonate fuel cells, J. Power Sources 112 (2002) 153–161, https://doi.org/10.1016/S0378-7753(02)00353-1.

[43] P. Biedenkopf, M. Spiegel, H.J. Grabke, The corrosion behaviour of iron and chromium in molten (Li0.62K0.38)2CO3, Electrochim. Acta 44 (1998) 683–692, https://doi.org/10.1016/S0013-4686(97)10191-8.

[44] L. Guo, Y. Yue, T.J. Pan, Z.F. Tang, W. Liu, Corrosion behavior of Ni-Al alloys beneath chlorides melt salt at 700 °C, Sol. Energy 184 (2019) 657–663, https://doi.org/10.1016/j.solener.2019.04.045.

[45] X.L. Wang, A.R. Huang, M.X. Li, W. Zhang, C.J. Shang, J.L. Wang, Z.J. Xie, The significant roles of Nb and Mo on enhancement of high temperature urea corrosion resistance in ferritic stainless steel 269 (2020), https://doi.org/10.1016/j.matlet.2020.127660.

[46] E. Sadeghimeresht, L. Reddy, T. Hussain, M. Huhtakangas, N. Markocsan, S. Joshi, Influence of KCl and HCl on high temperature corrosion of HVAF-sprayed NiCrAlY and NiCrMo coatings, Mater. Des. 148 (2018) 17–29, https://doi.org/10.1016/j.matdes.2018.03.048.

[47] L. Guo, Q. Liu, H. Yin, T.J. Pan, Z. Tang, Excellent corrosion resistance of 316 stainless steel in purified NaCl-MgCl2 eutectic salt at high temperature, Corros. Sci. 166 (2020) 108473, https://doi.org/10.1016/j.corsci.2020.108473.